

## CONDENSED MATTER PHYSICS

## Moiré ferroelectricity modulates light emission from a semiconductor monolayer

Dong Seob Kim<sup>1,2</sup>, Chengxin Xiao<sup>3</sup>, Roy C. Dominguez<sup>4</sup>, Zhida Liu<sup>1,2</sup>, Hamza Abudayyeh<sup>1,2</sup>, Kyoungpyo Lee<sup>1,2</sup>, Rigo Mayorga-Luna<sup>4</sup>, Hyunsue Kim<sup>1,2</sup>, Kenji Watanabe<sup>5</sup>, Takashi Taniguchi<sup>6</sup>, Chih-Kang Shih<sup>1,2</sup>, Yoichi Miyahara<sup>4,7</sup>, Wang Yao<sup>3</sup>, Xiaoqin Li<sup>1,2\*</sup>

Semiconductor moiré superlattices, characterized by their periodic spatial light emission, unveil a new paradigm of engineered photonic materials. Here, we show that ferroelectric moiré domains formed in a twisted hexagonal boron nitride (t-hBN) substrate can modulate light emission from an adjacent semiconductor MoSe<sub>2</sub> monolayer. The electrostatic potential at the surface of the t-hBN substrate provides a simple way to confine excitons in the MoSe<sub>2</sub> monolayer. The excitons confined within the domains and at the domain walls are spectrally separated because of a pronounced Stark shift. Moreover, the patterned light emission can be dynamically controlled by electrically gating the ferroelectric domains, introducing a functionality beyond other semiconductor moiré superlattices. Our findings chart an exciting pathway for integrating nanometer-scale moiré ferroelectric domains with various optically active functional layers, paving the way for advanced nanophotonics and metasurfaces.

## INTRODUCTION

While semiconductor monolayers such as transition metal dichalcogenides (TMDs) have already found many photonic applications such as optical modulators (1, 2), detectors (3, 4), and light-emitting devices (5, 6), a moiré superlattice consisting of a twisted bilayer offers a substantially expanded parameter space for tunable properties. With subwavelength periodic light emission patterns, semiconductor moiré superlattices are emerging as an innovative form of active metasurfaces. They feature prominent exciton resonances whose resonant energies, lifetimes, and transport all depend on the twist angle (7–9). However, many properties of moiré excitons change simultaneously, imposing undesirable constraints. For example, as the lateral confinement size reduces with an increasing twist angle, the exciton lifetime increases rapidly, likely leading to reduced quantum efficiency (10, 11).

Hexagonal boron nitride (hBN), a different class of van der Waals materials, is often used as passive encapsulation layers or tunnel barriers. It has become increasingly relevant as a photonic material for hosting quantum defect emitters (12, 13) or detecting ultraviolet light (14) or as a natural hyperbolic material in the midinfrared range (15, 16). Very recently, slid or twisted hBN (t-hBN) bilayers with a parallel interface have been found to exhibit ferroelectricity (17, 18). Furthermore, it has been suggested that the periodic electrostatic potential on the top t-hBN surface can alter the properties of an adjacent functional layer placed on top of the t-hBN substrate (19). In this case, the generation of the moiré potential is separated from the functional layer, offering greater flexibility.

Here, we explore a strategy to seamlessly integrate the ferroelectric (FE) functionality of a t-hBN with a light-emitting semiconductor monolayer. The electrostatic potential on the surface of the t-hBN confines excitons in an adjacent MoSe<sub>2</sub> monolayer. Those excitons confined within the domains and along the domain walls (DWs) are spectrally separated because of the Stark shift induced by an in-plane electric field (E-field) that is the strongest at the DWs. By correlating Kelvin probe force microscopy (KPFM) and optical microscopy experiments, we show that the spatial light emission pattern follows the moiré pattern of the t-hBN substrate. Through electric gating, one can erase and restore the FE domains. Consequently, the light emission from the MoSe<sub>2</sub> monolayer exhibits characteristic hysteresis behavior. Because the FE domain size is readily controlled by the twist angle, the light emission pattern can be modulated at a length scale far below the optical diffraction limit, charting a pathway for creating active metasurfaces (20, 21).

## RESULTS

We first explain the formation of FE domains in a t-hBN bilayer conceptually, as depicted in Fig. 1A. A natural hBN crystal consists of layers stacked in an AA' sequence, in which hexagonal lattices overlap, and B (N) atoms are vertically aligned with corresponding N (B) atoms in adjacent layers. In another energetically favorable AB or BA (Bernal) stacking configuration, in which hexagonal lattices laterally slide, the B (N) atoms in the upper layer align with the N (B) atoms in the lower layer, and the N (B) atoms in the upper layer are positioned above the vacant center of the hexagon in the lower layer. The spatial inversion symmetry is broken, leading to opposite polarization directions between AB and BA stacking, as indicated by the black arrows.

An array of FE domains with alternating polarization directions is formed in a t-hBN bilayer in which the domain size is readily controlled by the twist angle. These FE domains can be directly visualized via KPFM shown in Fig. 1B as an example. Details of the sample preparation and KPFM measurements can be found in Materials and Methods. The color contrast in a KPFM image represents

<sup>1</sup>Department of Physics and Center for Complex Quantum Systems, University of Texas at Austin, Austin, TX 78712, USA. <sup>2</sup>Center for Dynamics and Control of Materials and Texas Materials Institute, University of Texas at Austin, Austin, TX 78712, USA. <sup>3</sup>New Cornerstone Science Laboratory, Department of Physics, The University of Hong Kong, Hong Kong, China. <sup>4</sup>Department of Physics, Texas State University, San Marcos, TX 78666, USA. <sup>5</sup>Research Center for Electronic and Optical Materials, National Institute for Materials Science, 1-1 Namiki, Tsukuba 305-0044, Japan. <sup>6</sup>Research Center for Materials Nanoarchitectonics, National Institute for Materials Science, 1-1 Namiki, Tsukuba 305-0044, Japan. <sup>7</sup>Materials Science, Engineering and Commercialization Program (MSEC), Texas State University, San Marcos, TX 78666, USA.

\*Corresponding author. Email: elaineli@physics.utexas.edu

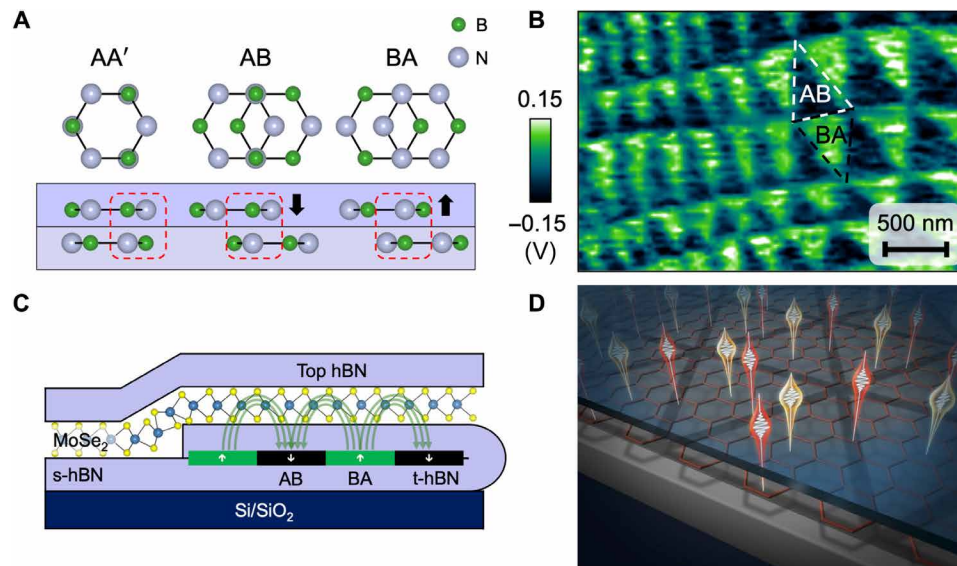


**Fig. 1. Moiré ferroelectric domains in t-hBN modulate light emission from an adjacent semiconductor layer.** (A) Top and side views of the hBN parallel interface at high-symmetry points. Inversion symmetry breaking leads to spontaneous polarization as indicated by down (up) black arrows corresponding to AB (BA) stacking. (B) KPFM image of the electrostatic moiré potential on the top surface of a t-hBN substrate. AB (BA) domains are marked by white (black) dashed triangles. (C) Sketch of a t-hBN/MoSe<sub>2</sub> monolayer/hBN van der Waals multilayer with alternating domains at the t-hBN interface. Green lines and arrows illustrate the E-field generated by the FE domains with the largest in-plane E-field at the DWs. s-hBN, slid hBN. (D) Illustration of spectral and spatial modulation of light emission from a semiconductor functional layer on top of a t-hBN substrate.

the electrostatic potential near the top surface of the t-hBN, which is related to polarization via

$$V(\mathbf{R}, z) \approx \text{sgn}(z) \frac{P(\mathbf{R})}{2\epsilon_0} e^{-G|z|} \quad (1)$$

where the net polarization is calculated from  $P(\mathbf{R}) = \int z' \Delta \rho(\mathbf{R}, z') dz'$ ,  $G = \frac{4\pi}{\sqrt{3}b}$ ,  $\mathbf{R}$  represents the lateral position vector,  $b$  characterizes the supercell size, and  $z$  is the vertical distance to the buried interface (19). The magnitude of  $P$  is  $2.01 \text{ pC m}^{-1}$  obtained from the first principles calculations. The surface potential extracted from KPFM measurements agrees remarkably well with the prediction of this theory (22). When a semiconductor functional layer is placed on top of a t-hBN substrate, the E-field (green lines in Fig. 1C) generated by the surface potential of the t-hBN can periodically modulate the spectral and spatial patterns of the semiconductor layer, as illustrated in Fig. 1D.

We calculate the in-plane E-field developed at the DWs due to an electrostatic potential drop between adjacent domains (Fig. 2A). In this example, we use a supercell size of 500 nm and a top thickness of t-hBN of 4.8 in Eq. 1. The side view of E-field vectors at the DW is plotted in Fig. 2B. The in-plane E-field decreases with an increasing distance  $z$  from the t-hBN interface. We hypothesize that the in-plane E-field at the DWs separates the electron and hole without dissociating the excitons in MoSe<sub>2</sub>, as illustrated in Fig. 2C. To verify this hypothesis, we conduct experiments by placing a MoSe<sub>2</sub> monolayer on a t-hBN substrate with large domains identified via the KPFM image shown in Fig. 2D.

Optical reflectivity measurements are taken from three locations across the DW, as indicated by the red arrow in Fig. 2D. The derivatives of reflectance spectra are displayed in Fig. 2E [corresponding photoluminescence (PL) spectra are displayed in fig. S3]. The three stacked spectra (bottom to top) are labeled by their respective locations shown in Fig. 2D. While spectra 1 and 3 taken within a domain feature one

exciton resonance, an additional exciton resonance is observed in spectrum 2 taken from a region that overlaps with the DW (the full optical spectra with finer steps are provided in fig. S4). We fit these resonances using Lorentzian functions (solid lines in Fig. 2E). The  $X_0$  exciton resonance measured within the AB and BA domains (spectra 1 and 3) exhibits a small energy shift of  $\sim 1 \text{ meV}$ . Because the spontaneous polarization directions are opposite in AB and BA domains, there may be some difference in how charge defects in MoSe<sub>2</sub> accumulate within each domain, causing this energy shift (23). The energy of  $X_0$  exciton in spectrum 2 lies in between the values in spectra 1 and 3. Considering the spatial resolution of  $\sim 1.5 \mu\text{m}$ , this intermediate energy likely derives from averaging over excitons residing in the two adjacent and opposite FE domains. We attribute the lower-energy exciton in spectrum 2 to the exciton Stark shift because of the in-plane E-field at the DW, as illustrated in Fig. 2C. The exciton Stark shift or the separation between the two resonances is  $\sim 3 \text{ meV}$  in this case.

To establish the Stark shift as the mechanism giving rise to the additional resonance at the DWs, we quantitatively evaluate the in-plane E-field. By measuring the potential profile ( $V_z$ ) across two domains with opposite polarization via KPFM and fitting it with a linear function across the DW width  $d_{\text{DW}}$ , we extract the E-field via  $F_x = \Delta V_s / d_{\text{DW}}$ . An example of this analysis is shown in Fig. 3A. Because the potential depth depends on the domain size, the in-plane E-field varies between regions with different domain sizes. To fully establish the correlation between the estimated in-plane E-field and the exciton Stark shift,  $E_{\text{shift}} = E_{X_0} - E_{X_{\text{Stark}}}$ , we investigate two samples (Fig. 3B) in which the MoSe<sub>2</sub> monolayer is separated from the t-hBN interface by 4.8 (square points) and 7.8 nm (triangle points), respectively. We also take measurements from several locations on each sample.

The in-plane E-field at the DW tends to separate the electron and hole along the field direction to lower the electrostatic energy at a smaller cost of binding energy. Thus, the overall exciton energy is

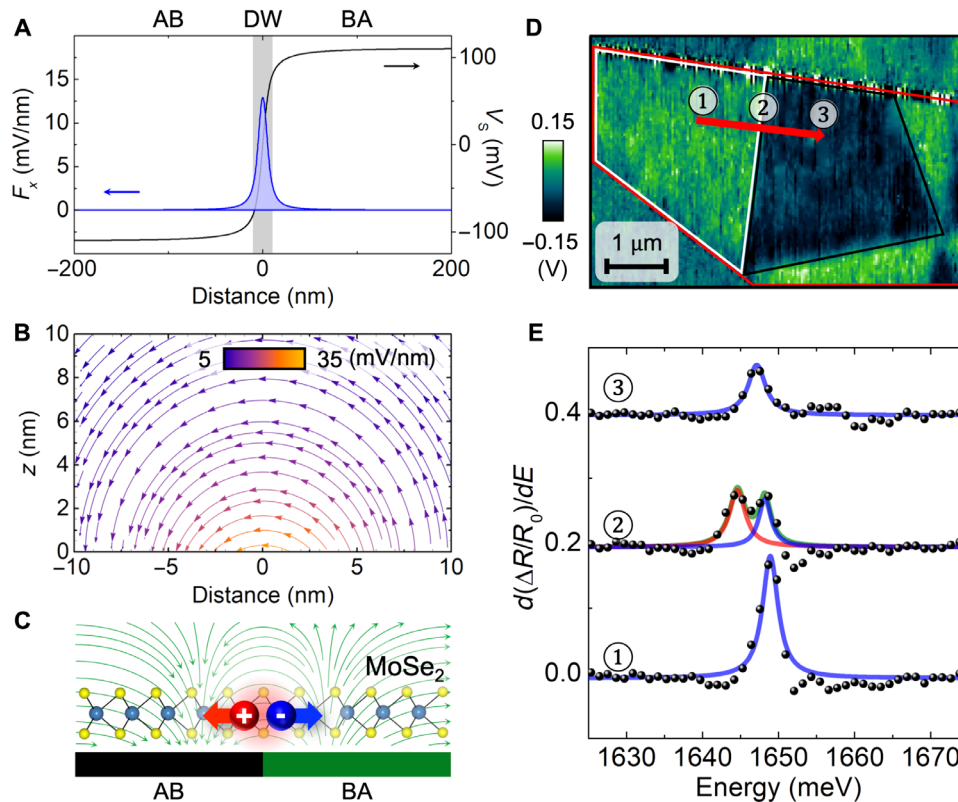


**Fig. 2. Stark-shifted excitons from MoSe<sub>2</sub> because of the in-plane E-field at the DWs of a t-hBN substrate.** (A) Calculated electrostatic potential (black) and in-plane E-field (blue) along a direction perpendicular to a DW. (B) Side view of E-field lines near the DW. The color represents the field strength. (C) The in-plane E-field at the DWs separates the electron and hole of an exciton and leads to a Stark-shifted exciton resonance. (D) KPFM image of a t-hBN substrate forming large domains. Optical spectra are taken from a MoSe<sub>2</sub> monolayer at three locations along the red arrow. (E) Derivative of reflectance contrast spectra from the MoSe<sub>2</sub> monolayer taken at three locations across two opposite and adjacent domains. The numbers correspond to the spots labeled in (D). One exciton resonance is observed within the AB and BA domains, while two resonances are observed at the DW.

lowered. This red shift of the Stark exciton is consistent with previous observations on the TMD monolayer embedded in a p-n junction (24, 25). Because of the absence of a permanent dipole moment, exciton energy does not shift linearly with the E-field. Instead, the lowest-order energy shift arises from the second-order perturbation theory, i.e., a quadratic Stark effect. This energy shift for 1s excitons can be expressed as

$$E_{\text{shift}} = -\frac{1}{2}\alpha F_x^2 \quad (2)$$

where  $\alpha$  is the exciton polarizability of MoSe<sub>2</sub> monolayers that we extract from a previous experiment (26). To display the data clearly, we only plotted the magnitude of the Stark shift in Fig. 3B. In other figures with original spectra, the red shift is clearly observed.

We calculate the Stark shift of the 1s excitons in MoSe<sub>2</sub> monolayers (blue dashed line) in Fig. 3B. Our experiment reports a larger Stark shift or higher exciton polarizability than previous studies (26, 27). This difference may originate from several reasons. First, there is a systematic error in extracting the in-plane E-field from KPFM measurements. In all measurements, the tip is kept at ~2 nm above the top surface of t-hBN substrates (details in Materials and Methods). This tip-sample separation is not negligible, considering the thin hBN layers (4.8 to 12 nm) used in assembling the twisted

substrates, thus contributing to underestimated in-plane E-fields. Second, a linear fit across the DW we chose may underestimate the in-plane E-field, while other reports have applied a nonlinear fit and chosen the steepest slope to extract the in-plane E-field (28).

Because the in-plane E-field and the  $X_{\text{Stark}}$  are only present at the DWs, one expects not only a spectral modulation but also a spatial modulation of the light emission from the functional semiconductor layer placed on top of the t-hBN with an array of FE domains (see fig. S7). We then compare the KPFM image (Fig. 3C) and confocal PL image (Fig. 3D) taken from a MoSe<sub>2</sub> monolayer placed on the t-hBN substrate. In Fig. 3D, we plot the integrated intensity ratio of  $X_{\text{Stark}}$  and  $X_0$  and observe a spatial correlation between the  $X_{\text{Stark}}$  intensity and the DWs (dashed red lines). There are some mismatched areas between the KPFM image and the PL map, which could be attributed to optically active defects (see fig. S8). As our measurements are constrained by the optical diffraction limit, we can only image ~500-nm or larger domains in our current experimental setup. In principle, light emission modulated by a van der Waals FE substrate can be patterned on a length scale far below the optical diffraction limit by simply increasing the twist angle.

Last, we demonstrate how an electric gate can modulate the exciton Stark shift from MoSe<sub>2</sub> by repeatedly erasing and restoring the FE domains of t-hBN substrates. To accomplish this, we fabricate a



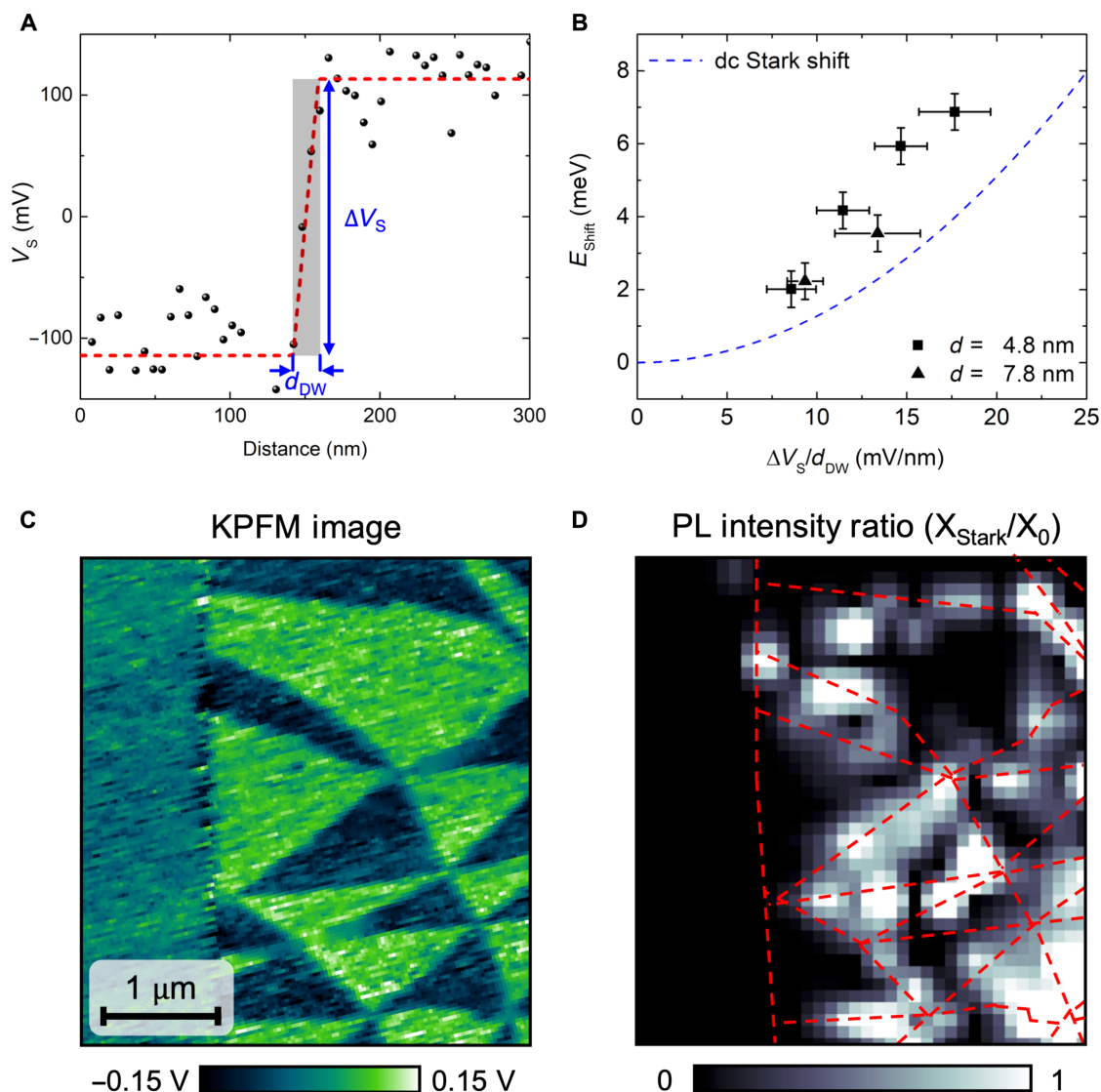


**Fig. 3. Spectral and spatial modulation of light emission from MoSe<sub>2</sub> by a t-hBN substrate.** (A) Electrostatic potential drops ( $\Delta V_s$  indicated by the vertical blue arrow) across the DW ( $d_{DW}$ ) of the t-hBN substrate, producing an in-plane E-field and causing an exciton Stark shift. The gray strip indicates a finite DW thickness ( $d_{DW}$ ). The dashed red line is a guide for the eye. (B) Summary of the exciton Stark shift as a function of the in-plane E-field, extracted from the KPFM measurements via  $\Delta V_s/d_{DW}$ . KPFM data are taken from two bare t-hBN substrates with different hBN thicknesses,  $d$ . The dashed blue line is the calculated exciton Stark shift. The error bars in the horizontal direction derive from both  $\Delta V_s$  and  $d_{DW}$ . The error bars in the vertical direction are fitting errors in extracting the exciton energy splitting for spectra taken across DWs. (C) KPFM image of the t-hBN substrate where PL spectra from an adjacent MoSe<sub>2</sub> monolayer are collected. (D) Spatial map of integrated PL intensity ratio of two exciton resonances  $X_{Stark}/X_0$ . The DWs are marked by red dashed lines.

dual-gate device structure as illustrated in Fig. 4A. The device is built on the same stacked layers measured in Fig. 1C in which the MoSe<sub>2</sub> monolayer is separated from the t-hBN interface by 12 nm. We measure a series of reflection spectra (Fig. 4B) as the vertically applied E-field;  $V_B/d_B$  is varied while keeping the MoSe<sub>2</sub> monolayer undoped (i.e., under the condition  $V_T/d_T + V_B/d_B = 0$ ). In the absence of a vertically applied E-field or a small E-field, exciton doublets are observed because of the exciton Stark shift at the DWs. When the vertically applied E-field is sufficiently large (i.e., above  $V_B/d_B = \pm 0.2$  V/nm), the exciton resonance subject to the Stark shift disappears. The observed change in optical spectra suggests that the DWs confining the Stark-shifted excitons are either erased or

considerably reconfigured by the electric gate. The shape and the dynamic evolutions of the FE domains under gating depend on multiple factors including the domain sizes and defects within the domain network (29). We summarize the exciton Stark shift as a function of the vertically applied E-field in Fig. 4D (see fig. S9 for more details). At a large applied E-field exceeding the critical value, the domain polarization is flipped or reconfigured (18, 29, 30) such that the electrostatic potential from the hBN substrate becomes constant, as illustrated in Fig. 4C. Consequently, the in-plane E-field vanishes and the  $X_{Stark}$  resonance disappears.

We observe the hysteresis behavior of exciton Stark shift in Fig. 4D as the gate voltage is swept forward (blue circles) and backward

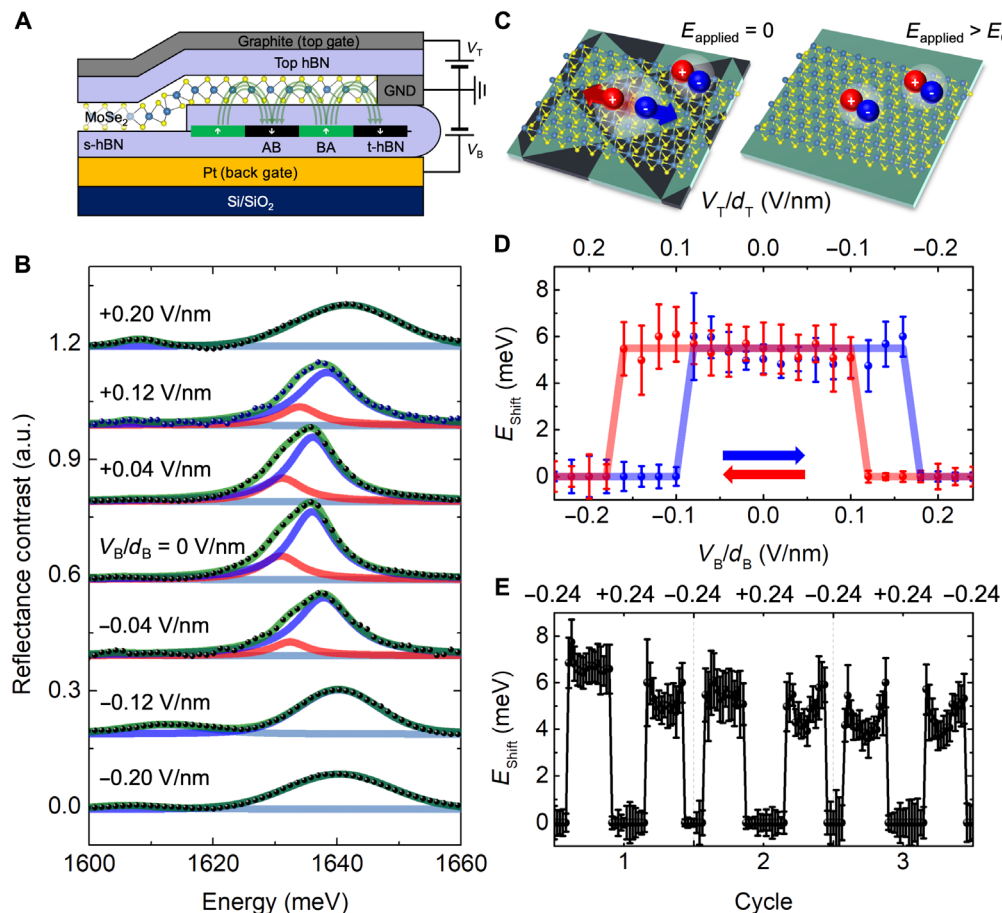


**Fig. 4. Hysteresis of the exciton Stark shift demonstrating the combined functionality of the FE t-hBN substrate with the MoSe<sub>2</sub> monolayer.** (A) Dual-gate device structure. A MoSe<sub>2</sub> monolayer is placed on a t-hBN substrate and encapsulated by a top hBN layer. A vertical E-field is applied by adjusting the back-gate voltage  $V_B$  and top gate simultaneously while keeping the monolayer undoped. GND, ground. (B) Reflectance spectra from the MoSe<sub>2</sub> monolayer placed on the t-hBN substrate at different applied vertical E-fields. The exciton Stark shift from the FE domains is observed at  $V_B/d_B = 0$  V nm<sup>-1</sup>. Above  $V_B/d_B = \pm 0.2$  V nm<sup>-1</sup> (top), the  $X_{\text{Stark}}$  peak disappears. Circles are measured data, and solid lines are Lorentzian fits. a.u., arbitrary units. (C) Illustration of field-driven switching of the FE domains of the t-hBN substrate as manifested via exciton resonances in the adjacent MoSe<sub>2</sub> monolayer. (D) Exciton Stark shift as a function of the applied E-field. The shift is constant until the resonance abruptly disappears above  $\pm 0.2$  V nm<sup>-1</sup>. Blue (red) circles are the measured exciton Stark shift as the vertically applied E-field sweeps forward (backward). Hysteresis behavior is characteristic of ferroelectricity from the t-hBN substrate. The solid lines are a guide for the eye. Error bars represent the root mean square errors from the Lorentzian fitting to optical spectra. (E) Multicycle switching of the FE domains manifested by the exciton Stark shift.

(red circles). This behavior is attributed to the ferroelectricity of the t-hBN substrate. We further demonstrated that this FE switching is reversible and robust over many switching cycles, as shown in Fig. 4E. The bottom gate and top gate are both changed in the range of  $-6$  to  $6$  V to keep the MoSe<sub>2</sub> layer charge neutral. The necessary switching voltage depends on the hBN thickness. The FE domain switching is measured via the exciton Stark shift. Over several cycles, the Stark-shifted exciton energy drifts, which likely arises from the DW distortions (fig. S9) (29, 31). Optical spectroscopy data are typically averaged over several domains, except in special cases where we intentionally choose to perform experiments along the DW of a large domain greater than several micrometers (e.g., Fig. 2, B and C). To understand how electronic bands may be modified between the DWs and domain interior regions, experiments with high-spatial-resolution techniques such as scanning transmission electron microscopy should be performed in the future.

## DISCUSSION

We discuss our findings in the context of previous studies. Heterostructures consisting of TMD thin layers placed on conventional FE substrates have been investigated previously (20, 32, 33). Conventional FE substrates usually have atomically sharp DWs (28, 34), and the in-plane E-field generated by a conventional FE substrate is so strong ( $\sim 400$  mV/nm) that excitons are often dissociated (33). In contrast, the in-plane E-field at the surface of t-hBN substrates studied is on the order of  $\sim 20$  mV/nm, which is much smaller than the binding energy ( $\sim 200$  meV) of excitons in TMD monolayers (35). Stark-shifted excitons are likely confined along the one-dimensional DWs and thus exhibit linear polarization (36). Furthermore, patterning FE domains requires advanced scanning probes or lithographic tools. The ability to easily create a regular array of FE domains with deep subwavelength length scales ( $\sim 10$  nm) and few-nanometer DW widths is a unique advantage of t-hBN in modulating atomically

thin semiconductors, establishing a platform for engineering active photonic materials (23) and possibly correlated states (37).

In conclusion, we demonstrate that a t-hBN substrate can modulate the light emission from an adjacent semiconductor layer both spectrally and spatially. The in-plane E-field introduced at the FE DWs is sufficiently large to induce a distinct Stark-shifted exciton resonance, similar to that found in semiconductor p-n junctions typically created with advanced lithograph tools (24, 25). The light emission can be further modulated by an electric gate that erases and restores the FE domains in the t-hBN. The hysteresis behavior observed in optical spectra demonstrates that the FE property of the t-hBN substrate is successfully combined with the light emission functionality of the semiconductor layer. Our findings open the exciting possibilities for designing metasurfaces and optoelectronic devices based on FE-hBN substrates. For example, FE tuning of exciton resonances may facilitate coupling to optical cavities, enabling polariton-based photonic devices.

## MATERIALS AND METHODS

### Sample preparation

We exfoliated hBN flakes using scotch tape onto 285-nm SiO<sub>2</sub>/Si substrates. After choosing a target hBN flake via microscope imaging, nitrogen gas is blown to facilitate the folding process (see fig. S1 for the detailed process). Samples typically fold along either zigzag or armchair directions. Those layers folded along the armchair direction exhibit an interface with broken inversion symmetry. Thus, ~50% of the folded hBN layers exhibit ferroelectricity as identified by KPFM images. After folding, the samples are annealed up to 400°C for 4 hours under vacuum (~10<sup>-7</sup> torr) to increase interface bonding by removing polymer residue. For the MoSe<sub>2</sub>/t-hBN device structure, prepatterned Pt/Ti is prepared by photolithography. Then, the t-hBN substrate is transferred using a 15% poly(propylene carbonate) solution and dissolved into anisole. Then, contact graphite, MoSe<sub>2</sub> monolayer, top hBN, and top gate graphite are transferred in the same way.

### KPFM measurements

KPFM measurements were performed using SmartSPM (Horiba) in two-pass frequency modulation KPFM (FM-KPFM) mode. All the data were taken by FM-KPFM mode. We used Pt-coated conductive cantilever probes with a nominal resonance frequency of 70 kHz and a spring constant of 2 N/m (OPUS 240AC-PP, Mikromasch) and the Au-coated cantilevers with supersharp diamond-like carbon tips with a nominal resonance frequency of 150 kHz and a spring constant of 5 N/m (BudgetSensors SHR150). In the FM-KPFM mode of SmartSPM, the resonance frequency shift of the mechanically excited oscillations (amplitude of 20 nm), which are caused by the electrostatic force gradient with respect to the tip-sample distance, is detected via the phase of the cantilever oscillations. The amplitude of the modulation of the phase, which is caused by applying an ac voltage (3 V, 1 kHz), is proportional to the difference between the applied dc bias voltage and the contact potential difference and is fed into a feedback controller to nullify the electrostatic force.

### Optical spectroscopy measurements

For optical reflectivity measurements at 14 K, a compact stabilized broadband light source was focused to a spot size of ~2 μm in

diameter using a 100× microscope objective. For PL measurements, a He-Ne laser was used, and the excitation power was kept below 5 μW to avoid local heating. The spatial mapping of PL was conducted in confocal geometry.

### Computational methods

Extending the formula in (19) to a nonrigid twist region by considering all the reciprocal vectors, we can calculate the static electric potential at any position

$$V(\mathbf{R}, z) \approx \sum_{\mathbf{G}} \frac{\tilde{P}(\mathbf{G})}{2\epsilon_0} e^{i\mathbf{G} \cdot \mathbf{R}} e^{-|\mathbf{G}|z} \quad (3)$$

where  $\tilde{P}(\mathbf{G})$  is the Fourier component of the electric dipole  $P(\mathbf{R}) = \int \Delta\rho(\mathbf{R}, z)zdz$ , with  $\Delta\rho$  denoting the differential charge density, and  $\mathbf{G}$  is the moiré reciprocal vector. The strong lattice reconstruction in the marginally twisted hBN results in a narrow DW between AB and BA stacking. Former ab initio study (38) shows that the DW width of strained bilayer hBN is around 8 to 10 nm. Thus, we calculated the electric potential and the E-field in Fig. 1 using Eq. 3 with triangular modified  $P(\mathbf{R})$  and 8-nm DW width.

### Supplementary Materials

This PDF file includes:

Figs. S1 to S9

### REFERENCES AND NOTES

1. K. L. Seyler, J. R. Schaibley, P. Gong, P. Rivera, A. M. Jones, S. Wu, J. Yan, D. G. Mandrus, W. Yao, X. X., Electrical control of second-harmonic generation in a WSe<sub>2</sub> monolayer transistor. *Nat. Nanotechnol.* **10**, 407–411 (2015).
2. Z. Sun, A. Martinez, F. Wang, Optical modulators with 2D layered materials. *Nat. Photonics* **10**, 227–238 (2016).
3. O. Lopez-Sanchez, D. Lembke, M. Kayci, A. Radenovic, A. Kis, Ultrasensitive photodetectors based on monolayer MoS<sub>2</sub>. *Nat. Nanotechnol.* **8**, 497–501 (2013).
4. B. W. H. Baugher, H. O. H. Churchill, Y. Yang, P. Jarillo-Herrero, Optoelectronic devices based on electrically tunable p-n diodes in a monolayer dichalcogenide. *Nat. Nanotechnol.* **9**, 262–267 (2014).
5. J. S. Ross, P. Klement, A. M. Jones, N. J. Ghimire, J. Yan, D. G. Mandrus, T. Taniguchi, K. Watanabe, K. Kitamura, W. Yao, D. H. Cobden, X. Xu, Electrically tunable excitonic light-emitting diodes based on monolayer WSe<sub>2</sub> p-n junctions. *Nat. Nanotechnol.* **9**, 268–272 (2014).
6. F. Withers, O. Del Pozo-Zamudio, A. Mishchenko, A. P. Rooney, A. Gholinia, K. Watanabe, T. Taniguchi, S. J. Haigh, A. K. Geim, A. I. Tartakovsky, K. S. Novoselov, Light-emitting diodes by band-structure engineering in van der Waals heterostructures. *Nat. Mater.* **14**, 301–306 (2015).
7. N. P. Wilson, W. Yao, J. Shan, X. Xu, Excitons and emergent quantum phenomena in stacked 2D semiconductors. *Nature* **599**, 383–392 (2021).
8. D. Huang, J. Choi, C.-K. Shih, X. Li, Excitons in semiconductor moiré superlattices. *Nat. Nanotechnol.* **17**, 227–238 (2022).
9. K. F. Mak, J. Shan, Semiconductor moiré materials. *Nat. Nanotechnol.* **17**, 686–695 (2022).
10. J. Choi, W.-T. Hsu, L.-S. Lu, L. Sun, H.-Y. Cheng, M.-H. Lee, J. Quan, K. Tran, C.-Y. Wang, M. Staab, K. Jones, T. Taniguchi, K. Watanabe, M.-W. Chu, S. Gwo, S. Kim, C.-K. Shih, X. Li, W.-H. Chang, Moiré potential impedes interlayer exciton diffusion in van der Waals heterostructures. *Sci. Adv.* **6**, eaba8866 (2020).
11. J. Choi, M. Florian, A. Steinhoff, D. Erben, K. Tran, D. S. Kim, L. Sun, J. Quan, R. Claassen, S. Majumder, J. A. Hollingsworth, T. Taniguchi, K. Watanabe, K. Ueno, A. Singh, G. Moody, F. Jahnke, X. Li, Twist angle-dependent interlayer exciton lifetimes in van der Waals heterostructures. *Phys. Rev. Lett.* **126**, 047401 (2021).
12. T. T. Tran, K. Bray, M. J. Ford, M. Toth, I. Aharonovich, Quantum emission from hexagonal boron nitride monolayers. *Nat. Nanotechnol.* **11**, 37–41 (2016).
13. G. Grosso, H. Moon, B. Lienhard, S. Ali, D. K. Efetov, M. M. Furchi, P. Jarillo-Herrero, M. J. Ford, I. Aharonovich, D. Englund, Tunable and high-purity room temperature single-photon emission from atomic defects in hexagonal boron nitride. *Nat. Commun.* **8**, 705 (2017).

14. A. Maity, S. J. Grenadier, J. Li, J. Y. Lin, H. X. Jiang, Hexagonal boron nitride neutron detectors with high detection efficiencies. *J. Appl. Phys.* **123**, 044501 (2018).
15. S. Dai, Z. Fei, Q. Ma, A. S. Rodin, M. Wagner, A. S. McLeod, M. K. Liu, W. Gannett, W. Regan, K. Watanabe, T. Taniguchi, M. Thiemens, G. Dominguez, A. H. Castro Neto, A. Zettl, F. Keilmann, P. Jarillo-Herrero, M. M. Fogler, D. N. Basov, Tunable phonon polaritons in atomically thin van der Waals crystals of boron nitride. *Science* **343**, 1125–1129 (2014).
16. J. D. Caldwell, A. V. Kretinin, Y. Chen, V. Giannini, M. M. Fogler, Y. Francescato, C. T. Ellis, J. G. Tischler, C. R. Woods, A. J. Giles, M. Hong, K. Watanabe, T. Taniguchi, S. A. Maier, K. S. Novoselov, Sub-diffractive volume-confined polaritons in the natural hyperbolic material hexagonal boron nitride. *Nat. Commun.* **5**, 5221 (2014).
17. K. Yasuda, X. Wang, K. Watanabe, T. Taniguchi, P. Jarillo-Herrero, Stacking-engineered ferroelectricity in bilayer boron nitride. *Science* **372**, 1458–1462 (2021).
18. M. Vizner Stern, Y. Waschitz, W. Cao, I. Nevo, K. Watanabe, T. Taniguchi, E. Sela, M. Urbakh, O. Hod, M. Ben Shalom, Interfacial ferroelectricity by van der Waals sliding. *Science* **372**, 1462–1466 (2021).
19. P. Zhao, C. Xiao, W. Yao, Universal superlattice potential for 2D materials from twisted interface inside h-BN substrate. *NPJ 2D Mater. Appl. Ther.* **5**, 38 (2021).
20. G. Wu, B. Tian, L. Liu, W. Lv, S. Wu, X. Wang, Y. Chen, J. Li, Z. Wang, S. Wu, H. Shen, T. Lin, P. Zhou, Q. Liu, C. Duan, S. Zhang, X. Meng, S. Wu, W. Hu, X. Wang, J. Chu, J. Wang, Programmable transition metal dichalcogenide homojunctions controlled by nonvolatile ferroelectric domains. *Nat. Electron.* **3**, 43–50 (2020).
21. A. Forbes, M. de Oliveira, M. R. Dennis, Structured light. *Nat. Photon.* **15**, 253–262 (2021).
22. D. S. Kim, R. C. Dominguez, R. Mayorga-Luna, D. Ye, J. Embley, T. Tan, Y. Ni, Z. Liu, M. Ford, F. Y. Gao, S. Arash, K. Watanabe, T. Taniguchi, S. Kim, C.-K. Shih, K. Lai, W. Yao, L. Yang, X. Li, Y. Miyahara, Electrostatic moiré potential from twisted hexagonal boron nitride layers. *Nat. Mater.* **23**, 65–70 (2024).
23. M. Cho, B. Datta, K. Han, S. B. Chand, P. C. Adak, S. Yu, F. Li, K. Watanabe, T. Taniguchi, J. Hone, J. Jung, G. Grosso, Y. D. Kim, V. M. Menon, Moiré exciton polaron engineering via twisted hBN. *Nano Lett.* **25**, 1381–1388 (2025).
24. M. Massicotte, F. Vialla, P. Schmidt, M. B. Lundberg, S. Latini, S. Haastrop, M. Danovich, D. Davydovskaya, K. Watanabe, T. Taniguchi, V. I. Fal'ko, K. S. Thygesen, T. G. Pedersen, F. H. L. Koppens, Dissociation of two-dimensional excitons in monolayer WSe<sub>2</sub>. *Nat. Commun.* **9**, 1633 (2018).
25. D. Thureja, A. Imamoglu, T. Smoleński, I. Amelio, A. Popert, T. Chervy, X. Lu, S. Liu, K. Barmak, K. Watanabe, T. Taniguchi, D. J. Norris, M. Kroner, P. A. Murthy, Electrically tunable quantum confinement of neutral excitons. *Nature* **606**, 298–304 (2022).
26. K. Xiao, T. Yan, C. Xiao, F.-R. Fan, R. Duan, Z. Liu, K. Watanabe, T. Taniguchi, W. Yao, X. Cui, Exciton-exciton interaction in monolayer MoSe<sub>2</sub> from mutual screening of Coulomb binding. *ACS Nano* **18**, 31869–31876 (2024).
27. T. G. Pedersen, Exciton Stark shift and electroabsorption in monolayer transition-metal dichalcogenides. *Phys. Rev. B* **94**, 125424 (2016).
28. J. Gonnissen, D. Batuk, G. F. Nataf, L. Jones, A. M. Abakumov, S. Van Aert, D. Schryvers, E. K. H. Salje, Direct observation of ferroelectric domain walls in LiNbO<sub>3</sub>: Wall-meanders, kinks, and local electric charges. *Adv. Funct. Mater.* **26**, 7599–7604 (2016).
29. K. Ko, A. Yuk, R. Engelke, S. Carr, J. Kim, D. Park, H. Heo, H.-M. Kim, S.-G. Kim, H. Kim, T. Taniguchi, K. Watanabe, H. Park, E. Kaxiras, S. M. Yang, P. Kim, H. Yoo, Operando electron microscopy investigation of polar domain dynamics in twisted van der Waals homobilayers. *Nat. Mater.* **22**, 992–998 (2023).
30. X. Wang, K. Yasuda, Y. Zhang, S. Liu, K. Watanabe, T. Taniguchi, J. Hone, L. Fu, P. Jarillo-Herrero, Interfacial ferroelectricity in rhombohedral-stacked bilayer transition metal dichalcogenides. *Nat. Nanotechnol.* **17**, 367–371 (2022).
31. L. Molino, L. Aggarwal, V. Enaldiev, R. Plumadore, V. I. Fal'ko, A. Luican-Mayer, Ferroelectric switching at symmetry-broken interfaces by local control of dislocations networks. *Adv. Mater.* **35**, e2207816 (2023).
32. B. Wen, Y. Zhu, D. Yudistira, A. Boes, L. Zhang, T. Yidirim, B. Liu, H. Yan, X. Sun, Y. Zhou, Y. Xue, Y. Zhang, L. Fu, A. Mitchell, H. Zhang, Y. Lu, Ferroelectric-driven exciton and trion modulation in monolayer molybdenum and tungsten diselenides. *ACS Nano* **13**, 5335–5343 (2019).
33. P. Soubelet, J. Klein, J. Wierzbowski, R. Silvili, F. Sigger, A. V. Stier, K. Gallo, J. J. Finley, Charged exciton kinetics in monolayer MoSe<sub>2</sub> near ferroelectric domain walls in periodically poled LiNbO<sub>3</sub>. *Nano Lett.* **21**, 959–966 (2021).
34. Z. Xiao, S. Poddar, S. Ducharme, X. Hong, Domain wall roughness and creep in nanoscale crystalline ferroelectric polymers. *Appl. Phys. Lett.* **103**, 112903 (2013).
35. M. Goryca, J. Li, A. V. Stier, T. Taniguchi, K. Watanabe, E. Courtade, S. Shree, C. Robert, B. Urbaszek, X. Marie, S. A. Crooker, Revealing exciton masses and dielectric properties of monolayer semiconductors with high magnetic fields. *Nat. Commun.* **10**, 4172 (2019).
36. L. Gu, L. Zhang, S. Felsenfeld, R. Ma, S. Park, H. Jang, T. Taniguchi, K. Watanabe, Y. Zhou, Quantum confining excitons with electrostatic moiré superlattice. arXiv:2501.11713 (2025).
37. N. Kiper, H. S. Adlong, A. Christianen, M. Kroner, K. Watanabe, T. Taniguchi, A. Imamoglu, M. Kroner, K. Watanabe, T. Taniguchi, A. Imamoglu, Confined trions and Mott-Wigner states in a purely electrostatic moiré potential. *Phys. Rev. X* **15**, 011049 (2025).
38. A. V. Lebedev, I. V. Lebedeva, A. A. Knizhnik, A. M. Popov, Interlayer interaction and related properties of bilayer hexagonal boron nitride: Ab initio study. *RSC Adv.* **6**, 6423–6435 (2016).

# Acknowledgments

**Funding:** The experiments are primarily supported by NSF MRSEC DMR-2308817 (to D.S.K.), Army Research Office W911NF-23-1-0364 (to K.L.), and NSF ECCS-2130552 (to Z.L. and H.A.). D.S.K. is partially supported by the NSF Designing Materials to Revolutionize and Engineer our Future (DMREF) program via grant DMR-2118806. X.L. gratefully acknowledges support from the Welch Foundation Chair F-0014. C.X. and W.Y. acknowledge support by RGC of HKSAR (AoE/P-701/20, HKU SRF52122-7505) and the New Cornerstone Science Foundation. The work by R.C.D. and R.M.-L. is supported by the NSF Partnership for Research and Education in Materials (PREM) (NSF award DMR-2122041). Y.M. acknowledges the support by the NSF CAREER (DMR-2044920) and NSF MRI (DMR-2117438) grants. The collaboration between X.L. and C.-K.S. is enabled by the National Science Foundation through the Center for Dynamics and Control of Materials, an NSF MRSEC under cooperative agreement nos. DMR-1720595 and DMR-2308817, which also supported the user facility where part of the experiments was performed. C.K.S. acknowledges support from the NSF (grant no. DMR-2219610), the Welch Foundation (F-2164), and the US Air Force (grant no. FA2386-21-1-4061). K.W. and T.T. acknowledge support from the JSPS KAKENHI (grant nos. 20H00354, 21H05233, and 23H02052) and World Premier International Research Center Initiative (WPI), MEXT, Japan.

**Author contributions:** D.S.K. and X.L. conceived the project. D.S.K. fabricated samples with assistance from K.L. D.S.K. carried out optical measurements with H.A. and Z.L.'s help, and R.C.D. and R.M.-L. performed atomic force microscopy and KPFM measurements. Electrical gating measurements were done by D.S.K. with contributions from H.K. and Z.L. K.W. and T.T. synthesized hBN single crystals. C.X. and W.Y. proposed the theoretical model and performed the calculation. D.S.K. analyzed the data with contributions from C.X. The first draft of the manuscript was written by D.S.K., C.-K.S., Y.M., W.Y., and X.L. All authors contributed to discussions. **Competing interests:** The authors declare that they have no competing interests.

**Data and materials availability:** All data needed to evaluate the conclusions in the paper are present in the paper and/or the Supplementary Materials.

Submitted 11 October 2024

Accepted 3 April 2025

Published 9 May 2025

10.1126/sciadv.adt7789